energies

MDPI

Article

Energy Shaping Control for Wireless Power Transfer System in Automatic Guided Vehicles

Wenjie Chen [1], Jia Liu [2,3,*], Si Chen [1] and Liyan Zhang [1]

[1] School of Automation, Wuhan University of Technology, Wuhan 430070, China; shine1994@foxmail.com (W.C.); oh_anita@163.com (S.C.); zlywhut@whut.edu.cn (L.Z.)
[2] College of Control Science and Engineering, Institute of Cyber-Systems and Control, Zhejiang University, Hangzhou 310027, China
[3] State Key Laboratory of Industrial Control Technology, Zhejiang University, Hangzhou 310027, China
* Correspondence: liujia1019@zju.edu.cn; Tel.: +86-180-0072-3096

Received: 13 March 2020; Accepted: 29 May 2020; Published: 9 June 2020

Abstract: This paper proposes an energy shaping controller of a DC/DC converter for automatic guided vehicles (AGVs) wireless power transfer (WPT). A transformer is inserted after the LCC topology to improve the transfer power, and the DC/DC boost converter is added before this topology to obtain desired systematic power dynamically. The system power transfer model is derived based on the idea of voltage transformation and the desired power can be implemented indirectly through regulating desired output voltage of DC/DC converter. With the proposed controller, this WPT system will have a much better dynamic performance and the effective working time can be increased significantly. Furthermore, this paper proposes dynamical regulation strategy for output power to get real time target power according to the charging curve of the battery. Simulation and experimental results verified the control performance of the proposed control scheme. A WPT prototype with power up to 1.65 kW was built, and 92.12% efficiency from DC power source to battery load is achieved, which is 4% higher than that obtained by the conventional PID method.

Keywords: wireless power transfer (WPT); automatic guided vehicles (AGVs); DC/DC converter; energy shaping control

1. Introduction

With the advantages of strong adaptability, high flexibility and automatic cruise, automatic guided vehicles (AGVs), also referred to as mobile robots with guidance lane, have been widely applied in automated and intelligent logistics industry [1]. Nowadays, AGVs have played an important role in logistics and transportation, automatic processing, mechanical assembly and other related fields. However, the battery needs to be recharged and energized cycle by cycle, resulting in low utilization rate and high use cost [2]. At present, traditional charging systems require plug-in operation and there are some potential security issues. In order to realize automatic charging and solve the safety problems, it has great economic value to adopt new charging method to increase the effective working time of AGVs [3,4].

In recent years, wireless power transfer (WPT) has drawn more and more attention [2,5,6]. With the characteristics of flexible charging position and freedom to plug the charger, WPT is regarded as a practical charging technical solution. It is a trend to apply WPT to energize AGVs [7–9]. Making use of the parking gap, continuous operation can be implemented by intermittent charging [10]. AGVs pick energy from the primary coil over the air without parking and stopping for manual charging. Therefore, the effective working time and utilization rate can be increased fundamentally [11,12].

In the wireless charging system, the compensation circuit is composed of a loosely coupled transformer and certain external passive inductors or capacitors. The largest transfer power can be obtained when the system works at resonance frequency [13,14]. Figure 1 shows four basic resonant compensation circuits, which are divided from the different series and parallel combinations: series–series (SS), series–parallel (SP), parallel–series (PS) and parallel–parallel (PP). In order to obtain a higher design degree, more compensation elements are added to achieve higher order compensation circuit. With the characteristics of load-independent current source and high efficiency, the double-sided LCC resonant compensation network is outstanding among these compensation circuits [15–17]. By adjusting the parameters of the secondary LCC compensation circuit, zero voltage switch (ZVS) can be realized in the inverter, which can not only improve the reliability of the system, but also reduces the system loss greatly [15,16,18].

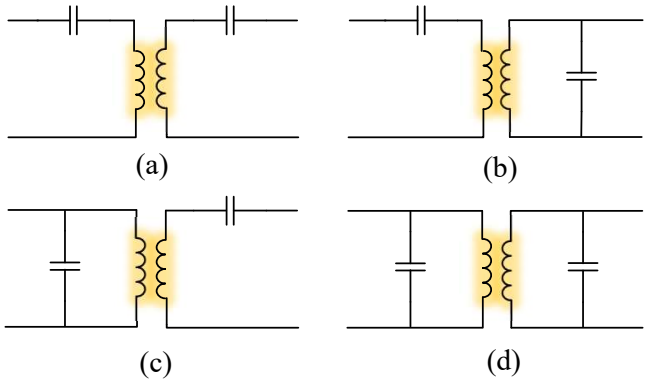

Figure 1. Four basic compensation circuits. (**a**) series–series (SS). (**b**) series–parallel (SP). (**c**) parallel–series (PS). (**d**) parallel–parallel (PP).

The magnetic coil is another significant concern in WPT [19,20]. As the most common and simplest structure, circular coupling coil is widely used by many researchers as the magnetic coupling coil for energy transmitter [20,21]. Generally, the magnetic cores laid under the coil are adopted to concentrate magnetic, and then aluminum plate is fixed as the outer layer to reduce the leakage magnetic flux. As an ideal single-sided magnetic coil, the ferrite core on one side of the coil forms the most magnetic flux, resulting in a flexible and convenient installation position. Therefore, the loss on the aluminum plate caused by magnetic leakage is very small. However, the maximum coupling height of circular coil is only about a quarter of the coil diameter, which is not beneficial to practical application. In order to solve this problem, double-D (DD) coil composed of two rectangular coils is introduced in [22]. The maximum coupling height is proportional to half of the coil length, then a higher coupling coefficient can be obtained with a smaller size coil [23,24].

Although the WPT technology has been widely applied in electric vehicles, the wireless charging of AGVs in the warehouse still need to be further studied. In [2,10,17,25], WPT systems for AGVs on receiver side control are proposed. A buck converter cascaded on the receiver side [25], which is adjusted by a PI regulator to maintain constant current output [2,17]. Making use of the DC/DC converter to maintain the equivalent load resistance, [10] proposes a new move and charge system for AGVs. In order to save space on AGVs side, a PI controlled phase shift full bridge inverter on the primary side is presented in [11]. However, considering safety, the working voltage of AGVs is usually 12 V, 24 V, or 48 V. The charging power is proportional to both side voltage of the compensation network [16], kWs level charging power seems not easy to be achieved. In this paper, a transformer and a boost converter are cascaded to front and back of the LCC topology, respectively, to improve the transfer power. The control method for AGVs system is another significant aspect. Numerous control methods have been proposed for the DC/DC converter. Compared with the other nonlinear control methods, energy shaping control via interconnection and damping assignment passivity-based control (IDA-PBC) has been regarded as the most effective practical nonlinear controller due to its simplicity,

efficiency and ease of implementation. The global stability of PBC for the DC/DC converter has been proved [26]. Taking the parasitic resistors into consideration, a output feedback PBC is proposed to achieve desired output voltage [27]. However, the controller is not easy to be implemented. For a SS compensated WPT system, a sliding mode control scheme is designed to track the maximum energy efficiency [28].

This paper aims to verify the energy shaping controller for the primary sided DC/DC converter of the WPT system in AGVs. By using port-controlled Hamiltonian system (PCHS) and IDA-PBC [28,29], the proposed controller ensures the stability and fast response of the system to achieve target output power dynamically. This goal can be implemented indirectly by regulating the voltage of the DC/DC converter. The power transfer model can be derived from the idea of voltage transformation. Moreover, since the working state of the battery and target power changes dynamically during the charging process, it is not an easy task to design a controller to satisfy needed systematic power in real-time. In order to regulate the transfer power based on demanded power, a dynamical regulation strategy for charging power is also presented to work with energy shaping controller. Simulation and experimental results show that this proposed controller has a better dynamic performance compared with PID algorithm in [17]. A WPT prototype output power of 1.65 kW for AGVs was built, and 92.12% efficiency from DC power source to battery load was achieved.

This paper is organized as follows. In Section 2, the structure and topology of the wireless charging system for AGVs are analyzed, and the system power transfer model of this system is derived. Section 3 proposes the energy shaping controller with dynamical regulation of output power. The simulation and experimental results are shown in Section 4, and some conclusions are given in Section 5.

2. Modelling Wireless Charging System

Figure 2 shows the structure of wireless charging system for AGVs, which is composed of AGV side and power transfer side. The AGV side consists of secondary compensation circuit, AC/DC rectifier, WIFI communication module and the receiver coil installed on the bottom of AGV. The power transfer side is composed of primary compensation circuit, DC/AC inverter, AC/DC converter, DC/DC converter, DSP controller and certain transmitter coils pre-placed at the temporary stops on the guided lane. The DSP controller includes WIFI communication module. The whole system starts to work when the AGV arrives and stops at this parking points, then AGVs can be energized cycle and cycle during the parking gap. The gap is generally as short as 1 to 1.2 s.

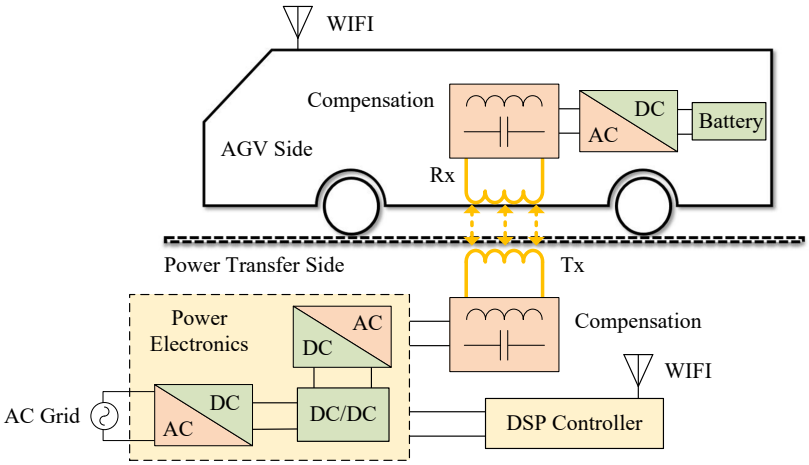

Figure 2. The structure of wireless charging system for automatic guided vehicles (AGVs).

As shown in Figure 3, L_1 and L_2 are the transmitter coil and the receiver coil, respectively. L_{f1}, C_{f1} and C_1 are the primary resonant inductor, capacitor and compensation capacitor, respectively. L_{f2}, C_{f2} and C_2 are the secondary resonant inductor, capacitor and compensation capacitor, respectively. ω and

f denote the operating angular frequency and operating frequency, respectively. The relation can be represented as ω=$2\pi f$. T represents the transformer, and the ratio is $n : 1 : 1$, where $n = 4$. This transformer together with two diodes D_1 and D_2 forms the full wave rectifier circuit, i.e., the AC/DC rectifier. M denotes the mutual inductor between the two coils. v_{AB} is the input voltage of the compensation circuit, and v_{ab} is the input voltage of the full wave rectifier circuit.

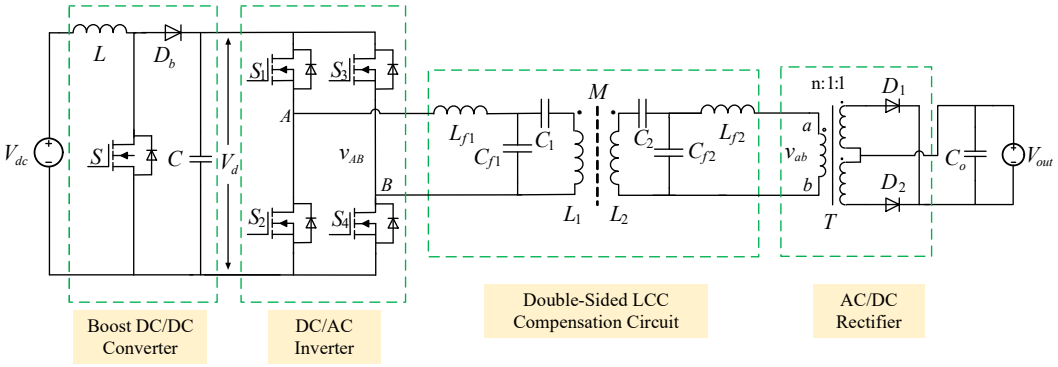

Figure 3. Structure of the wireless charing system for AGV.

In order to form a resonant topology, the parameters of compensation circuit are designed as follows [15]:

$$\begin{cases} \omega L_1 - (\omega C_1)^{-1} - (\omega C_{f1})^{-1} = 0 \\ \omega L_{f1} - (\omega C_{f1})^{-1} = 0 \\ \omega L_2 - (\omega C_2)^{-1} - (\omega C_{f2})^{-1} = 0 \\ \omega L_{f2} - (\omega C_{f2})^{-1} = 0 \end{cases} \tag{1}$$

In this resonance double-sided LCC topology, inductor series with capacitor between the primary side and the secondary side can be regarded as a low-pass filter. Then a concise characteristic of the proposed compensation topology can be given by analyzing the first-order harmonics of the square voltage waveform at the switching frequency. As for the high-order harmonics, the interaction through the primary side and secondary side can be neglected. The first-order component of input and output voltage between the two sides of this topology determines the transfer power of this topology.

Therefore, when the system works in the resonant operating condition [15,16], the transfer power of the double-sided LCC circuit can be expressed by

$$P = \frac{M}{\omega L_{f1} L_{f2}} V_{AB} V_{ab} \tag{2}$$

where V_{ab} denotes the first-order rms value of the output voltage before the rectifier, and V_{AB} represents the first order rms value of input voltage, i.e., the output voltage of the DC/AC inverter. The desired transfer power can be implemented by regulating V_{AB} and V_{ab}. In this paper, a transformer after the LCC topology is designed to improve the transfer power through increasing V_{ab} by n times. The DC/DC boost converter is inserted before LCC topology to regulate V_{AB} for the desired systematic power dynamically.

Figure 4 shows the voltage transformation process of the primary side. The DC/DC block denotes the DC/DC boost converter and the DC/AC block denotes the full bridge inverter. V_{dc} represents the input voltage of this boost converter and the V_d represents the output voltage of the boost converter, i.e., the input voltage of the full bridge inverter.

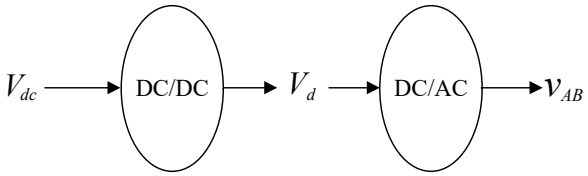

Figure 4. Voltage transformation process of the primary side.

For the DC/DC boost converter, according to the voltage-second balance principle, we have

$$V_{\mathrm{dc}}d + (V_{dc} - V_d)(1 - d) = 0 \tag{3}$$

where d denotes the duty ratio of the boost converter. Therefore, the voltage ratio is given by

$$\frac{V_d}{V_{dc}} = \frac{1}{1 - d} \tag{4}$$

The output voltage of the DC/AC inverter is a square wave, and the density of the positive and negative pulses in pulse width modulation (PWM) is denoted by δ. To realize the ZVS of the DC/AC converter [30], we let $\delta = 1$. Then the $v_{AB}(t)$ can be expressed as follows:

$$v_{AB}(t) = \begin{cases} -V_d, -\frac{T}{2} \le t < 0 \\ V_d, 0 \le t \le \frac{T}{2} \end{cases} \tag{5}$$

According to Fourier series [31], any periodic function can be expressed by the infinite order of sine and cosine function, which is written as follows

$$f(t) = \frac{a_0}{2} + \sum_{n=1}^{\infty} [a_m \cos(m\omega t) + b_m \sin(m\omega t)] \tag{6}$$

where $a_m = \frac{2}{T}\int_{t_0}^{t_0+T} f(t)\cos(m\omega t)dt$ and $b_m = \frac{2}{T}\int_{t_0}^{t_0+T} f(t)\sin(m\omega t)dt$. a_0 denotes the amplitude of $f(t)$ and the period is T.

Combining (5) and (6), a_m and b_m satisfies

$$\begin{aligned} a_m &= \tfrac{2}{T}\int_{-\frac{T}{2}}^{0} (-V_d)\cos(m\omega t)dt + \tfrac{2}{T}\int_{0}^{\frac{T}{2}} V_d \cos(m\omega t)dt = 0 \\ b_m &= \tfrac{2}{T}\int_{-\frac{T}{2}}^{0} (-V_d)\sin(m\omega t)dt + \tfrac{2}{T}\int_{0}^{\frac{T}{2}} V_d \sin(m\omega t)dt = \tfrac{2V_d}{m\omega T}[2 - 2\cos(m\pi)] \end{aligned}$$

where

$$b_m = \begin{cases} \frac{4V_d}{m\pi}, m = 1, 3, 5 \cdots \\ 0, m = 0, 2, 4 \cdots \end{cases}$$

Therefore, $v_{AB}(t)$ can be written in the form of Fourier series as

$$v_{AB}(t) = \frac{4}{m\pi} V_d \sum_{m=1,3,5\cdots}^{\infty} \sin(m\omega t) \tag{7}$$

Then, we get the first-order value of the output voltage of the DC/AC inverter

$$v_{AB\_1st}(t) = \frac{4}{\pi} V_d \sin(\omega t) \tag{8}$$

The rms value of $v_{AB\_1st}(t)$ can be obtained

$$V_{AB} = \frac{v_{AB\_1st}(t)}{\sqrt{2}} = \frac{2\sqrt{2}}{\pi} V_d \tag{9}$$

Similarly to the AGV side, the voltage relationship is shown in Figure 5, where $v_{ab}(t)$ and V_{out} represent the input voltage of the AC/DC rectifier and the voltage of the battery, respectively. $v_{ab}(t)$ is a passive voltage generated by the working mode of D_1 and D_2. Its amplitude is determined by V_{out}. Then $v_{ab}(t)$ can be described as

$$v_{ab}(t) = \begin{cases} -nV_{out}, -\frac{T}{2} \leq t < 0 \\ nV_{out}, 0 \leq t \leq \frac{T}{2} \end{cases} \tag{10}$$

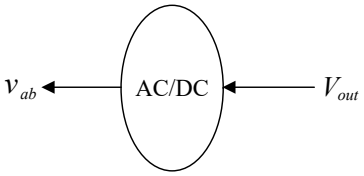

Figure 5. Voltage transformation process of the AGV side.

Similar to the primary side, the relationship between the voltage of the battery and V_{ab} can be derived

$$V_{ab} = \frac{v_{ab\_1st}}{\sqrt{2}} v_{ab\_1st} = \frac{2\sqrt{2}}{\pi} nV_{out} \tag{11}$$

Therefore, by using (2), (4), (9) and (11), the system transfer power has the form

$$P = \frac{8n}{\pi^2} \frac{MV_{out}}{\omega L_{f1} L_{f2}} V_d = \frac{8n}{\pi^2} \frac{MV_{out}}{\omega L_{f1} L_{f2}} \frac{V_{dc}}{1-d} \tag{12}$$

Refer to (12), it indicates that the real-time systematic transfer power can be achieved by adjusting the duty ratio d, which can be implemented indirectly through regulating the input voltage of double-sided LCC topology, i.e., the output voltage of the DC/DC boost converter.

3. Energy Shaping Control with Dynamical Regulation of Charging Power

The topology of the DC/DC Boost converter is shown in Figure 6. To avoid the high peak current and lower power density which exist in discontinuous conduction mode (DCM), the converter is designed to work in the continuous conduction mode (CCM). Then the average model is given by

$$\begin{cases} \frac{di_L}{dt} = \frac{V_{dc}}{L} - \frac{(1-d)}{L} v_d \\ \frac{dv_d}{dt} = -\frac{v_d}{CR} + \frac{(1-d)}{C} i_L \end{cases} \tag{13}$$

where L and C denote the inductor and the output capacitor, respectively. R denotes the load of this converter. i_L and v_d represent the inductor current and the voltage on capacitor, respectively, and V_{dc} denotes the input voltage.

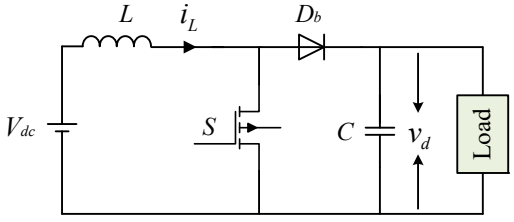

Figure 6. The topology of the DC/DC boost converter.

3.1. Energy Shaping via IDA-PBC

The DC/DC Boost converter model (13) takes the port-controlled hamiltonian (PCH) form [27]

$$\begin{cases} \dot{x} = [J(x) - R(x)] \cdot \frac{\partial H(x)}{\partial x} + \zeta + g(x)u \\ y = g^{\mathrm{T}}(x) \frac{\partial H(x)}{\partial x} \end{cases} \tag{14}$$

where $x \in R^n$ represents the state vector; $J(x)$, $R(x)$ denote the interconnection and dissipation matrices, where $J(x) = -J(x)^{\mathrm{T}}$ and $R(x) = R(x)^{\mathrm{T}}$. $H(x)$ is the total stored energy function and $g(x)$ denotes the input matrices. ζ represents the outside force. u and y are the control input and the output function, respectively.

In the view of energy, the energy function of the PCH system can be obtained

$$H(x) = \frac{1}{2} x^{\mathrm{T}} Q x \tag{15}$$

where $x = (x_1, x_2)^{\mathrm{T}} = (L \cdot i_L, C \cdot v_d)^{\mathrm{T}}$, the variables x_1 and x_2 represent the inductor magnetic flow and the charge in the capacitor, respectively. $Q = diag\{1/L, 1/C\}$ respects the topology parameters. Therefore, by using (13) and (14), we can obtain

$$J(x) = \begin{pmatrix} 0 & -1 \\ 1 & 0 \end{pmatrix}, R(x) = \begin{pmatrix} 0 & 0 \\ 0 & 1/R \end{pmatrix},$$

$$\zeta = (V_{dc}, 0)^{\mathrm{T}}, g(x) = \begin{pmatrix} x_2/C, -x_1/L \end{pmatrix}^{\mathrm{T}}.$$

In this paper, assuming that x^* is an desired fixed point of x, the desired energy function of system (14) can be derived as follows

$$H_d(x) = \frac{1}{2} x_e^{\mathrm{T}} Q x_e \tag{16}$$

where $x_e := x - x^*$.

Assume there are matrices $J_d(x) = -J_d(x)^{\mathrm{T}}$, $R_d(x) = -R_d(x)^{\mathrm{T}} \geq 0$, $H_d(x)$ is such that

$$x^* = \arg\min H_d(x) \tag{17}$$

Then, with help of energy shaping, the closed-loop system (14) takes the PCH form

$$\dot{x} = [J_d(x) - R_d(x)] \frac{\partial H_d(x)}{\partial x} \tag{18}$$

with a stable fixed point x^*. The largest invariant set can be described as

$$\left\{ x \in R^n | \frac{\partial H_d^{\mathrm{T}}(x)}{\partial x} R_d \frac{\partial H_d(x)}{\partial x} = 0 \right\} \tag{19}$$

the largest invariant set only contains $\{x^*\}$. Refer to (16), the energy function $H_d(x) \geq 0$. The time derivative of $H_d(x)$ with respect to x is derived as follows

$$\dot{H}_d(x) = \frac{\partial H_d^{\mathrm{T}}(x)}{\partial x} [J_d(x) - R_d(x)] \frac{\partial H_d(x)}{\partial x} = -\frac{\partial H_d^{\mathrm{T}}(x)}{\partial x} R_d(x) \frac{\partial H_d(x)}{\partial x} \leq 0 \tag{20}$$

therefore, $H_d(x)$ can be a candidate Lyapunov function. According to the La Salle's principle and the conclusion (19), considering that x^* is a stable fixed point, the closed-loop system is asymptotically stable. Combining (14) with (18), we get

$$[J_d(x) - R_d(x)] \frac{\partial H_d(x)}{\partial x} = [J(x) - R(x)] \frac{\partial H(x)}{\partial x} + \zeta + g(x)u \tag{21}$$

Assuming that $H_d(x) = H(x) + H_a(x)$, $J_d(x) = J(x) + J_a(x)$, $R_d(x) = R(x) + R_a(x)$, where $H_a(x)$, $J_a(x)$ and $R_a(x)$ denote the interconnection, dissipation matrices and energy function injected into the system through control. $u = d$ denotes the duty ratio of the boost converter. Assuming that $J_d(x) = 0$, $R_d(x) = diag(r_1, 1/r_2)$, and $K(x) = \partial H_a(x)/\partial x = \partial H_d(x)/\partial x - \partial H(x)/\partial x = \begin{pmatrix} -x_1^*/L & -x_2^*/C \end{pmatrix}^{\mathrm{T}}$, (21) can be calculated as follows

$$\begin{cases} \frac{x_1^*}{L} r_1 = \frac{r_1}{L} x_1 + \frac{d-1}{C} x_2 + V_{dc} \\ \frac{x_2^*}{C} \frac{1}{r_2} = \frac{1-d}{L} x_1 + \frac{1}{r_2 C} x_2 - \frac{1}{RC} x_2 \end{cases} \tag{22}$$

where $r_1 > 0$ and $r_2 > 0$ are the injected impedances. They are be able to shape the energy of the dynamic system. Substituting x_1, x_2 in (22), the duty ratio can be derived

$$d = \frac{v_d - V_{dc} + r_1(I_d^* - i_L)}{v_d} \tag{23}$$

where I_L^* is the desired points of i_L.

Assuming that the loss in the DC/DC converter is neglected, the relationship between the steady-state value of output voltage and inductor current can be obtained by principle of conservation for energy. When the system reaches a stable state, we get

$$I_L^* = \frac{V_d^{*2}}{V_{dc} R} \tag{24}$$

where V_d^* represents the desired points of v_d. Therefore, by using (23) and (24), the duty ratio can be expressed as

$$d = \frac{v - V_{dc} + r_1(V_d^{*2}/V_{dc}R - i_L)}{v_d} \tag{25}$$

Remark 1. *From the description of energy shaping control* (25)*, the duty ratio is obtained according to the sampling current and voltage. The time complexity of this controller is* $\boldsymbol{O}(1)$*, and it can provide a real-time application to solve the practical engineering problem.*

3.2. Dynamic Regulation of Charging Power

During the charging process, systematic needed power changes in different charging status. In order to meet the requirement of the demanded power, a dynamic regulation strategy for charging power is also presented to operate with energy shaping controller. The rated output voltage of the vehicle battery is 21.2∼28.2 V, and the capacity is 40 Ah. For convenience of indicating the charge current, 1 C is defined as the charging current which is equal to the capacity of the battery in numerical terms, i.e., the charging current is 1 C when the charging current is 40 A. In order to realize a fast charging speed, the rated maximum charging current is set at 1.7 C, i.e., the maximum charging current is 68 A.

Referring to the charging current depicted in Figure 7, the charging process can be divided into four stages: precharge, constant current charge (CCC), constant voltage charge (CVC) and end charging. According to the voltage of the battery, the charging process switches dynamically among these four stages. V_1 is set to 18 V and V_2 is set to 25.2 V. Therefore, by detecting the voltage of the battery, the required charging current can be obtained from the charging curve of the battery. The wireless charging system for AGVs mainly works in two stages: CCC and CVC. When this system works in CCC stage, the demand power will increase with the increasing battery voltage and the

charging current is 1.7 C. If the voltage of the battery is greater than V_2, this system will switch to work on CVC stage, and the demand current and power will decrease with the increasing battery voltage.

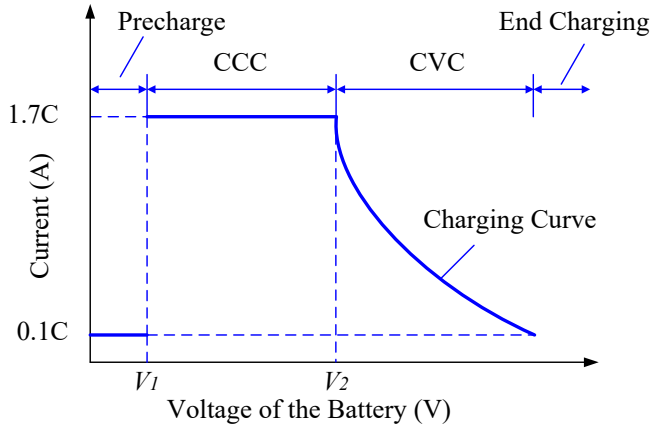

Figure 7. Charging curve of the battery.

According to (12), a desired transfer power can be obtained by regulating the desired output voltage of DC/DC converter dynamically. When the AGV arrives at the temporary stops, the charging information, such as state of charge (SOC) and voltage of the battery, can be sent to the digital signal processor (DSP) controller using the WIFI communication modules. According to the voltage of the battery, the real-time demand charging current I^*_{out} can be obtained through Figure 7. Then we get the required output power $P^* = I^*_{out} V_{out}$ dynamically. The corresponding desired output voltage V^*_d can be obtained by using (12). The control block diagram of wireless charging system is shown in Figure 8.

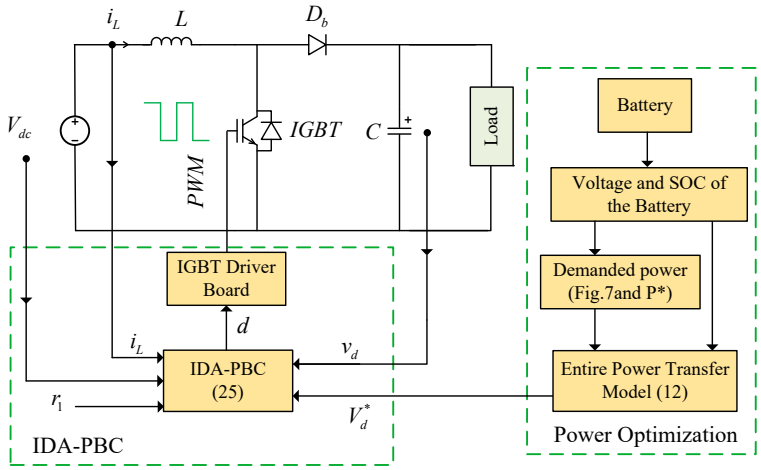

Figure 8. The control block diagram of wireless charging system for AGV.

4. Simulation and Experiment

In this section, the control performance of this proposed controller for the WPT system has been tested in PLECS. The real hardware experimental setups are implemented to further validate this proposed controller and dynamical regulation strategy for charging power. The parameters of the WPT system are shown in Table 1.

4.1. Simulation Results

In order to validate the dynamic performance of the proposed IDA-PBC, tests have been done in PLECS. The tests include two process, i.e., step-up process and step-down process. The step-up process represents that the desired output voltage of the DC/DC boost converter changes from 550 V to 650 V,

where the 550 V is initial stable state and the 650 V is the final stable state. Similarly, the step-down process represents that the desired output voltage of the DC/DC boost is set from 600 V to 450 V. In order to further verify the proposed method, a fair comparison test has been done using PID algorithm in [17]. The parameters are designed using Discrete PID Controller of Matlab.

Table 1. Parameters of the Wireless Charging System.

Parameter	Value	Unit
Primary resonant inductor L_{f1}	47.10	μH
Secondary resonant inductor L_{f2}	46.81	μH
primary resonant capacitor C_{f1}	74.44	nF
Secondary resonant capacitor C_{f2}	74.90	nF
Primary compensation capacitor C_1	97.93	nF
Secondary compensation capacitor C_2	101.74	nF
Primary coil L_1	82.90	μH
Secondary coil L_2	81.27	μH
Mutual inductor M	26.28	μH
Resonant frequency f	85	kHz
Nominal gap of two coils h	50	mm
Voltage of the battery V_{out}	21.2∼28.2	V
Switching frequency of the DC/DC converter f_s	20	kHz
Capacitor of the DC/DC converter C	400	μF
Inductor of the DC/DC converter L	2500	μH
Input voltage V_{dc}	310	V

The simulation results of the step-down process are shown in Figure 9. When it comes to PID algorithm, the transient time of this process is 48.3 ms. Also we can see that the minimum voltage of this process is 446 V and the percentage overshoot is 0.89%. Compared with PID algorithm, when using IDA-PBC method, the transient time is 23.6 ms. Also it is clear that the minimum voltage of this process is 449 V and the percentage overshoot is 0.22%.

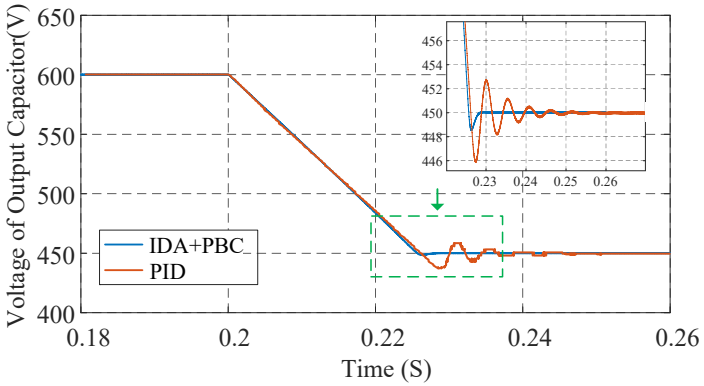

Figure 9. Simulation results of dynamic performance in step-down process test.

The simulation results of step-up process are shown in Figure 10. In the performance of PID algorithm, the transient time of this process is 30 ms. We can know that the maximum voltage of this process is 664 V and the percentage overshoot is 2.15%. When it comes to IDA-PBC algorithm, the transient time is 11 ms. The maximum voltage of this process is 652 V and the percentage overshoot is 0.31%. The simulation results are shown in Table 2.

A charging process includes a step-down process and a step-up process. According to the simulation results, the saved total transient time is 43.7 ms during a charging process using the energy shaping control method. Assuming that the parking gap is 1 s and the charging power is constant during a charging process, then more energy about 4.37% can be transferred using this proposed

charging method. In conclusion, a large transient time can be saved and super much more energy can be transferred.

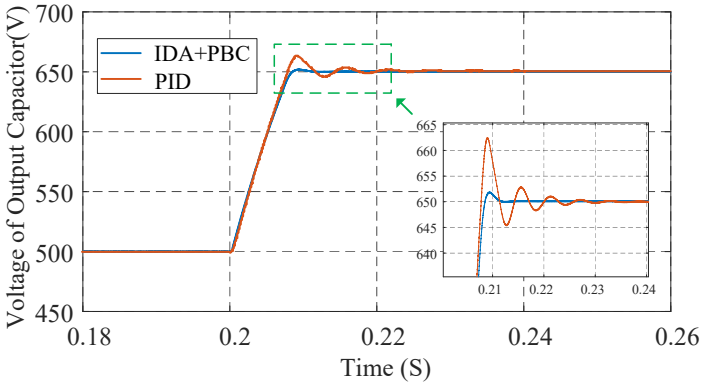

Figure 10. Simulation results of dynamic performance in step-down process test.

Table 2. Comparison of Simulation Results.

Charging Process	Specifications	PID	IDA-PBC
Step-down	Transient time	48.3 ms	23.6 ms
	Percentage overshoot	0.89%	0.22%
Step-up	Transient time	30 ms	11 ms
	Percentage overshoot	2.15%	0.31%

The simulation results shows that a better dynamic performance can be achieved and the transient time is half of that of PID algorithm. During the charging process, the charging state and demand current change dynamically. As shown in Figure 8, the demanded charging power can be implemented by regulating the output voltage of boost converter in real-time.

In order to verify the dynamic regulation of charging power, a dynamic regulation test has been done and the results are shown in Figure 11. In this test, the voltage of the battery changes dynamically. The initial voltage is 26 V, and it changes to 24 V at 0.3 s. At 0.5 s, it changes to 25.6 V finally. Refer to Figure 7, when the battery voltage is 26 V, the wireless charging system works in CVC mode and the reference charging current is 1.47 C. When the battery voltage changes to 24 V, the wireless charging system switches to work in CCC mode and the reference charging current is 1.7 C. Finally, battery voltage changes to 25.6 V at 0.5 s, then the wireless charging system works in CVC mode and the reference charging current is 1.54 C. In these three stages, the desired output voltage V_d^* are 550 V, 650 V and 616 V, respectively. The output powers are 1530 W, 1650 W and 1580 W, respectively. The above results verify the effectiveness of the dynamical regulation strategy.

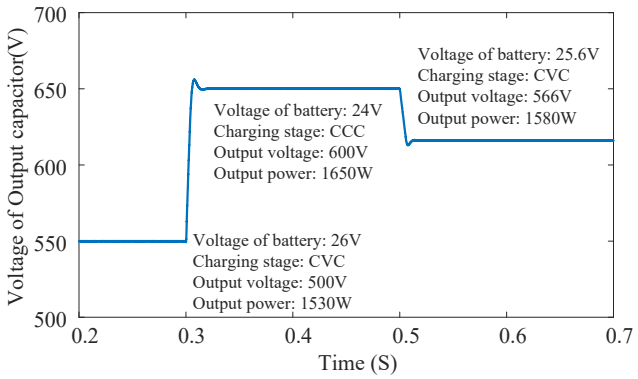

Figure 11. Simulation results of dynamical regulation.

4.2. Experimental Results

To verify the proposed controller, the real hardware experimental setups have been built. The overall experimental prototype of charging system are depicted in Figure 12a. Figure 12b shows the experimental prototype of primary transmitter cabinet and Figure 12c shows the experimental prototype of secondary receiver cabinet. The electronic components used in the WPT system are shown in Table 3.

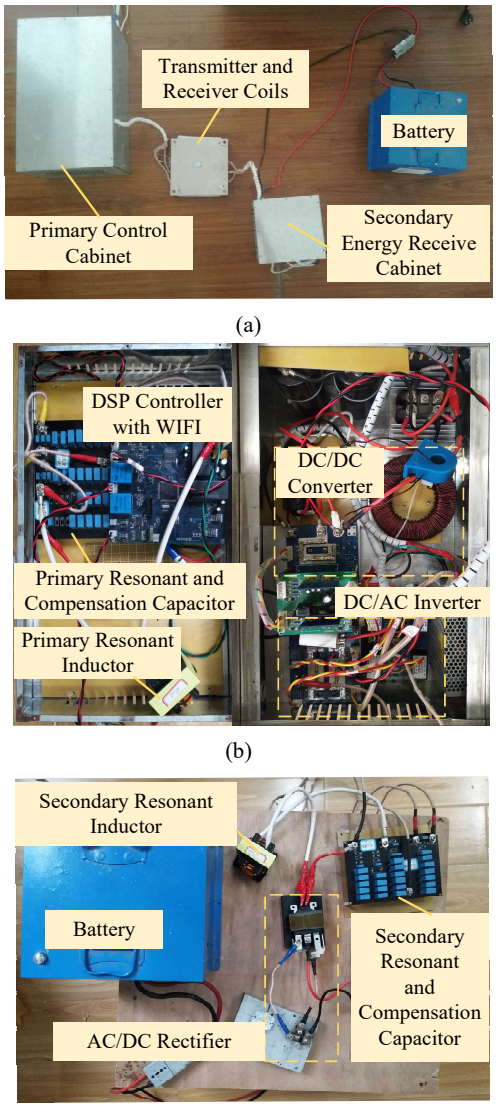

Figure 12. The experimental prototypes. (**a**) The experimental setup of charging system. (**b**) The experimental setup of transmitter cabinet. (**c**) The experimental setup of receiver cabinet.

Table 3. Electronic Components in Wireless Charging System.

Parts	Specifications	Quantity
Battery V_{out}	24 V/40 Ah	1
DSP controller	TMS320F28335	1
IGBT in boost converter S	IKW40N120H3	1
Diodes in boost converter D_b	40EPF06	1
IGBT driver board	DA102D1	1
Mosfets in DC/AC inverter S_1,S_2,S_3,S_4	SCH208KE	4
Diode in AC/DC rectifier D_1,D_2	DSEI 2*61-10B	1

4.2.1. Dynamic Performance Experiment

Similarly, the step-down process and step-up process tests are carried to verify the effectiveness of the proposed strategy. Figure 13 show the results of step-down process with two different methods. The results show that the transient time using PID and IDA-PBC are 42 ms and 20 ms, respectively. The experimental results of step-up process are shown in Figure 14. It shows that the transient time using PID and IDA-PBC are 36 ms and 14 ms, respectively. The experimental results show the same conclusion as previous simulation results that a fast dynamic response is achieved. This indicates that the saved total transient time is 44 ms and about 4.4% more energy can be transferred during a charging process.

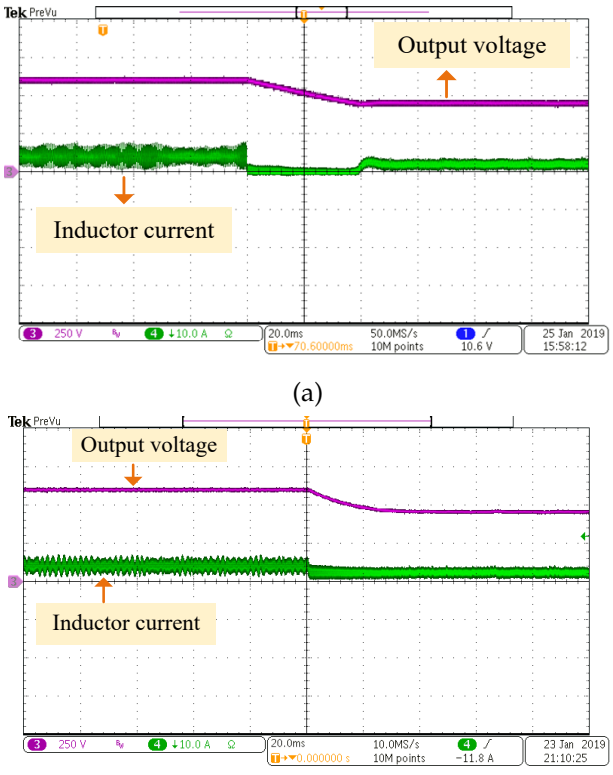

Figure 13. Experimental results of step-down process applied to two different methods. (**a**) PID. (**b**) Interconnection and damping assignment passivity-based control (IDA-PBC).

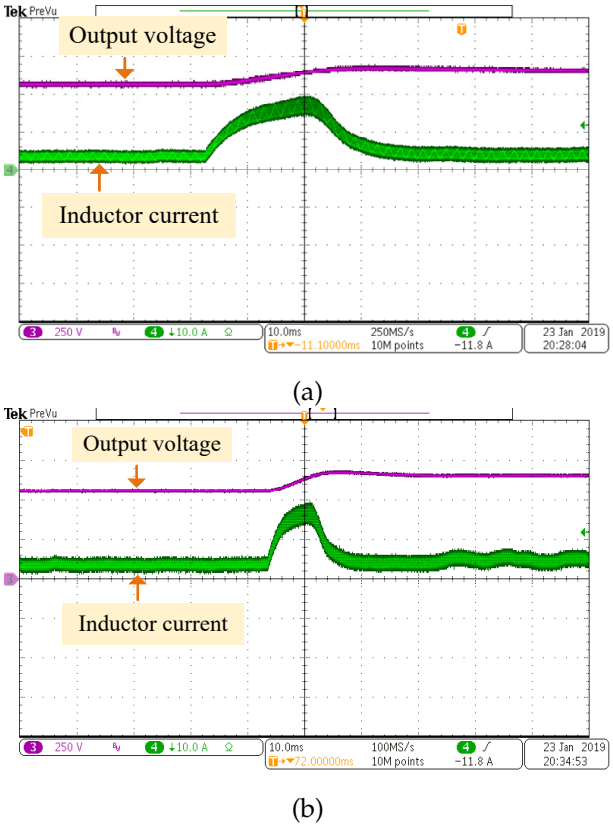

Figure 14. Experimental results of step-up process applied two different methods. (**a**) PID. (**b**) IDA-PBC.

4.2.2. Charging Power Efficiency

The charging power efficiency is another significant concern. Figure 15 shows the charging power efficiency of this wireless charging system at different transfer power point. The maximum transfer power is 1.65 kW, and the maximum transfer efficiency is 92.12%. The minimum transfer power is 0.195 kW, and the minimum transfer efficiency is 82.53%. Figure 15 shows that the transfer efficiency using IDA-PBC is 2∼4% is higher than that of the PID algorithm. The transfer efficiency is 4% higher when the transfer power is 0.4 kW. The results also indicate that a higher transfer efficiency can be obtained when the system achieves a larger charging power.

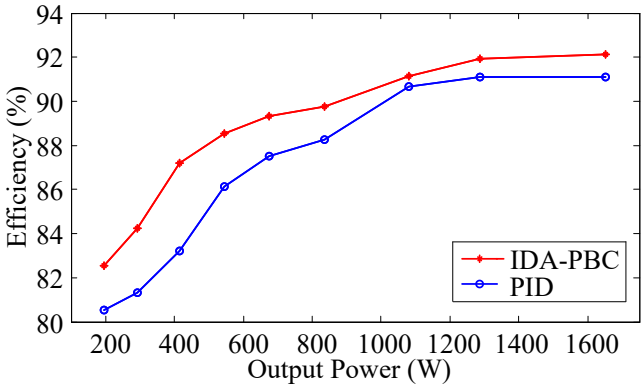

Figure 15. Efficiencies at different charging power.

5. Conclusions

In this paper, an energy shaping controller has been proposed. The novel control scheme aims to obtain the real-time desired power through dynamical regulation strategy for charging power. In order

to improve the charging power, a transformer is cascaded after the double-sided LCC topology. The voltage transformation model on primary side and secondary side have been presented, and the entire power transfer model has been derived. Simulation and experimental results validated the proposed control scheme, which have shown that the proposed controller can not only ensure the stability but also achieve fast response of the system. A 1.65 kW WPT prototype in AGVs has been built to verify the analysis results, and the measured efficiency from DC power source to battery load was as high as 92.12%.

Author Contributions: Conceptualization, W.C., J.L., S.C. and L.Z.; methodology, W.C.; software, W.C. and J.L.; validation, W.C., J.L. and S.C.; formal analysis, W.C.; investigation, W.C., J.L. and S.C.; resources, W.C., J.L., S.C. and L.Y.Z.; data curation, W.C., J.L. and S.C.; writing–original draft preparation, W.C.; writing–review and editing, W.C. and J.L.; visualization, W.C., J.L. and S.C.; supervision, J.L. and L.Z.; project administration, W.C., and J.L.; funding acquisition, W.C., J.L. and L.Z. All authors have read and agreed to the published version of the manuscript.

Funding: This work was supported by the National Natural Science Foundation of China under contract 61673306.

Conflicts of Interest: The authors declare no conflict of interest.

Abbreviations

The following abbreviations are used in this manuscript:

WPT	wireless power transfer
AGVs	automatic guided vehicles
IDA-PBC	Interconnection and damping assignment passivity-based control
PBC	passivity-based control
EVs	electric vehicles
SS	series–series
SP	series–parallel
PS	parallel–series
PP	parallel–parallel
ZVS	zero voltage switch
DD	double-D
PWM	pulse width modulation
CCM	continuous conduction mode
DCM	discontinuous conduction mode
PCH	port-controlled hamiltonian
CCC	constant current charge
CVC	constant voltage charge
SOC	state of charge
DSP	digital signal processor

References

1. Kongezos, V.K.; Allen, C.R. Wireless communication between AGVs (autonomous guided vehicles) and the industrial network CAN (controller area network). In Proceedings of the 2002 IEEE International Conference on Robotics and Automation (Cat. No.02CH37292), Washington, DC, USA, 11–15 May 2002; pp. 434–437.
2. Hao, Y.; Wang, J.; Liu, Y. Research on wireless power transfer system of automated guided vehicle based on magnetic coupling resonance. In Proceedings of the 2019 22nd International Conference on Electrical Machines and Systems (ICEMS), Harbin, China, 11–14 August 2019; pp. 1–4.
3. Umar, U.A.; Ariffin, M.K.A.; Ismail, N.; Tang, S.H. Hybrid multiobjective genetic algorithms for integrated dynamic scheduling and routing of jobs and automated-guided vehicle (AGV) in flexible manufacturing systems (FMS) environment. *Intern. J. Adv. Manuf. Technol.* **2015**, *8*, 2123–2141. [CrossRef]
4. Zhang, G.; Pan, Z. The application research of mobile robots and wireless sensor network in laser automatic guided vehicles. In Proceedings of the 2011 Third International Conference on Measuring Technology and Mechatronics Automation, Shangshai, China, 6–7 January 2011; pp. 708–711.

5. Huang, S.; Lee, T.; Li, W.; Chen, R. Modular on-road AGV wireless charging systems via interoperable power adjustment. *IEEE Trans. Ind. Electron.* **2019**, *66*, 5918–5928. [CrossRef]
6. Zhang, H.; Zhu, C.; Lu, F. A compact and low-distortion inductive charging system for automatic guided vehicles based on LCC compensation and integrated magnetic coupler. In Proceedings of the 2019 IEEE Transportation Electrification Conference and Expo (ITEC), Detroit, MI, USA, 19–21 June 2019; pp. 1–5.
7. Song, C.; Kim, H.; Jung, D.H.; Kim, J.J.; Kong, S.; Kim, J.; Ahn, S.; Kim, J.; Kim, J. Low EMF and EMI design of a tightly coupled handeld resonant magnetic field (HH-RMF) charger for automotive battery charging. *IEEE Trans. Electromagn. Compat.* **2016**, *4*, 1194–1206. [CrossRef]
8. Zaheer, A.; Covic, G.A.; Kacprazak, D. A bioplar pad in a 10 kHz 300-W distributed IPT system for AGV applications. *IEEE Trans. Ind. Electron.* **2014**, *7*, 3288–3301. [CrossRef]
9. Matsumoto, H.; Shibako, Y.; Neba, Y. Contacless power transfer syatem for AGVs. *IEEE Trans. Ind. Electron.* **2018**, *65*, 251–260. [CrossRef]
10. Jiang, C.; Chau, K.T.; Liu, C.; Lee, C.H.T.; Han, W.; Liu, W. Move-and-charge system for automatic guided vehicles. *IEEE Trans. Magn.* **2018**, *54*, 1–5. [CrossRef]
11. Trung, N.T.N.K.; Minh, T.T. Control the constant current/voltage charging mode in the wireless charging system for electric vehicle with LCC compensation circuit. In Proceedings of the 2019 IEEE Vehicle Power and Propulsion Conference (VPPC), Hanoi, Vietnam, 14–17 October 2019; pp. 1–5.
12. Miller, J.M.; Omer, O.C.; Madhu, C. Primary side power flow control of wireless power transfer for electric vehicle charging. *IEEE J. Emerg. Sel. Top. Power Electron.* **2014**, *3*, 147–162. [CrossRef]
13. Patil, D.; McDonough, M.K.; Miller, J.M.; Fahimi, B.; Balsara, P.T. Wireless power transfer for vehicular applications: Overview and challenges. *IEEE Trans. Transp. Electrif.* **2017**, *4*, 3–37. [CrossRef]
14. Tan, T.; Chen, K.; Jiang, Y.; Lin, Q.; Yuan, L.; Zhao, Z. A bidirectional wireless power transfer system control strategy independent of real-time wireless communication. *IEEE Trans. Ind. Appl.* **2019**, *56*, 1587–1598. [CrossRef]
15. Kan, T.; Lu, F.; Nguyen, T.D.; Mercier, P.P.; Mi, C.C. Integrated coil design for EV wireless charging systems using LCC compensation topology. *IEEE Trans. Power Electron.* **2018**, *33*, 9231–9241. [CrossRef]
16. Zhang, W.; Mi, C.C. A double-sided LCC compensation network and its tuning method for wireless power transfer. *IEEE Trans. Veh. Technol.* **2015**, *64*, 2261–2273.
17. Li, Z.; Zhu, C.; Jiang, J.; Song, K.; Wei, G. A 3-kW wireless power transfer system for sightseeing car supercapacitor charge. *IEEE Trans. Power Electron.* **2017**, *32*, 3301–3316. [CrossRef]
18. Pantic, Z.; Bai, S.; Lukic, S.M. ZCS LCC-compensated resonant inverter for inductive-power-transfer application. *IEEE Trans. Ind. Electron.* **2011**, *58*, 3500–3510. [CrossRef]
19. Zhang, F.; Zhang, J.; Qian, Y.J. A multi-node rechargeable algorithm via wireless charging vehicle with optimal traveling path in wireless rechargeable sensor networks. In Proceedings of the 2018 Tenth International Conference on Ubiquitous and Future Networks (ICUFN), Prague, Czech Republic, 3–6 July 2018.
20. Deng, J.; Li, W.; Nguyen, T.D.; Li, S.; Mi, C.C. Compact and efficient bipolar coupler for wireless power chargers: Design and analysis. *IEEE Trans. Ind. Electron.* **2011**, *30*, 6130–6140. [CrossRef]
21. Nguyen, T.; li, S.; Li, W.; Mi, C.C. Feasibility study on bipolar pads for efficient wireless power chargers. In Proceedings of the 2014 IEEE Applied Power Electronics Conference and Exposition-APEC 2014, Fort Worth, TX, USA, 16–20 March 2014; pp. 1676–1682.
22. Chen, Y.; Yang, N.; Yang, B.; Dai, R.; He, Z.; Mai, R.; Gao, S. Two-three-coil hybrid topology and coil design for WPT system charging electric bicycles. *IET Power Electron.* **2019**, *12*, 2501–2512. [CrossRef]
23. Zaheer, A.; Covic, G.A.; Kacprzak, D. Magnetic intergration of LCC compensation resonant converter for inductive power transfer applications. *IEEE Trans. Ind. Electron.* **2014**, *61*, 3288–3301. [CrossRef]
24. Zhang, Z.; Pang, H.; Georgiadis, A.; Cecati, C. Wireless Power Transfer - An Overview. *IEEE Trans. Ind. Electron.* **2019**, *4*, 1044–1058. [CrossRef]
25. Chen, W.; Chen, Q.; Zhang, L.; Long, R. Passivity-based controller of dynamic wireless power transfer system. In Proceedings of the 2019 34rd Youth Academic Annual Conference of Chinese Association of Automation (YAC), Jinzhou, China, 6–8 June 2019; pp. 381–386. [CrossRef]
26. Zeng, J.; Zhang, Z.; Qiao, W. An interconnection and damping assignment passivity-based controller for a DC/DC boost converter with a constant power load. *IEEE Trans. Ind. Appl.* **2014**, *50*, 2314–2322.
27. Ortega, R.; Garcia–Canseco, E. Interconnection and damping assignment passivity-based control: A survey. *Eur. J. Control* **2004**, *10*, 432–450. [CrossRef]

28. Son, Y.; Kim, I.H. Complementary PID controller to passivity-based nonlinear control of boost converters with inductor resistance. *IEEE Trans. Control Syst. Technol.* **2011**, *20*, 826–834. [CrossRef]
29. Petrovic, V.; Ortega, R.; Stankovic, A.M. Interconnection and damping assignment approach to control of PM synchronous motors. *IEEE Trans. Control Syst. Technol.* **2001**, *50*, 811–820. [CrossRef]
30. Li, H.; Fang, J.; Chen, S.; Wang, K.; Tang, Y. Pulse density modulation for maximum efficiency point tracking of wireless power transfer systems. *IEEE Trans. Power Electron.* **2018**, *33*, 5492–5501. [CrossRef]
31. Papula, L. *Papula Mathematische Formelsammlung*; Springer: Wiesbaden, Germany, 2017. [CrossRef]